Manipulation of Amorphous Precursors to Enhance Zeolite Nucleation

Journal:	*Faraday Discussions*
Manuscript ID	FD-ART-11-2021-000096
Article Type:	Paper
Date Submitted by the Author:	23-Nov-2021
Complete List of Authors:	Parmar, Deependra; University of Houston, Chemical and Biomolecular Engineering Niu, Zhiyin; University of Houston, Chemical and Biomolecular Engineering Liang, Yu; University of Houston, Chemical and Biomolecular Engineering Dai, Heng; University of Houston System, Rimer, Jeffrey; University of Houston, Chemical and Biomolecular Engineering

Manipulation of Amorphous Precursors to Enhance Zeolite Nucleation

Deependra Parmar[1], Zhiyin Niu[1], Yu Liang[1], Heng Dai[1], Jeffrey D. Rimer[1]*

[1] Department of Chemical and Biomolecular Engineering, University of Houston, Houston, TX, 77204, USA
* Email: jrimer@central.uh.edu

Abstract

Crystallization in media comprised of amorphous precursors is becoming a more common phenomenon for numerous synthetic, biological, and natural materials that grow by a combination of classical and nonclassical pathways. Amorphous phases can exhibit a wide range of physicochemical properties that may evolve during the course of nucleation and crystal growth. This creates challenges for establishing causal relationships between amorphous precursor properties and their effect(s) on the selection of mechanistic pathways of crystallization and ultimately the properties of the crystalline product. In this study we examine ways to manipulate the composition and colloidal stability of amorphous (alumino)silicate precursors that are prevalent in nanoporous zeolite syntheses. Changes in amorphous precursor properties are evaluated on the basis of their ability to enhance rates of crystal formation. Here we use fumed silica as the sole silicon source and examine the effects of infusing the source with an alkali metal, which serves as an inorganic structure-directing agent to facilitate the formation of porous crystal structures. We also assess the impact of adding a polymer additive, which reduces the colloidal stability of precursors wherein we posit the confined pockets of solution within interstitial spaces of precursor aggregates play an important role in regulating the rate of zeolite crystallization. Three commercially relevant zeolites (mordenite, SSZ-13, and ZSM-5) were selected for this study based on their diverse frameworks and methods of preparation. Our findings reveal that alkali infusion significantly reduces crystallization times for mordenite and SSZ-13, but has little impact on ZSM-5 synthesis. Conversely, we find that polymer addition markedly enhanced the rates of crystallization among all three zeolites, suggesting this method may be a general approach to reduce zeolite synthesis times. Given the relatively high costs associated with commercial zeolite production, identifying new methods to improve the efficiency of hydrothermal syntheses can have significant practical implications beyond the fundamental benefits of developing new routes to tailor nonclassical crystallization.

1. Introduction

The ubiquitous presence and important role(s) of amorphous precursors in crystallization spans numerous inorganic and organic systems.[1-6] Precursors can be diverse species that include (but are not limited to) oligomeric networks, clusters, and nanoparticles. They can function as sites for heterogeneous nucleation in two-step processes,[1, 7-9] serve as growth units in crystallization by particle attachment (CPA),[10, 11] or may be bystanders that regulate the supply of solute to/from the growth solution. One method of influencing crystal formation to achieve products with tailored physicochemical properties is through the manipulation of precursor structure and/or composition. Precursors are generally amorphous but can possess local structure as well as variations in composition, such as the degree of solvation or the occlusion of foreign species (e.g. ions, organics, etc.), Over the course of crystallization, it is also possible that precursors evolve in these properties with concomitant changes in their roles in nucleation and/or growth. Understanding causal relationships between precursor properties and crystallization mechanisms is nontrivial; however, it is recognized that developing improved knowledge of precursor assembly and their impact on pathways of crystal growth holds tremendous potential for crystal engineering.

One of the most complex systems of crystallization is that of zeolites, which are (alumino)silicates with multidimensional networks of nanopores.[12, 13] Zeolites are natural clays but are also produced synthetically for widespread industrial applications as catalysts, sieves, and sorbents for separations or ion exchange.[14-19] Zeolites crystallize with a broad range of Si/Al ratios and require the use of a structure-directing agent to facilitate the formation of cages/channels and/or compensate the negative charge of Al sites within the zeolite framework (i.e. function as extra-framework cations). Organics used for this purpose commonly possess quaternary ammonium moieties whereas organic-free syntheses often employ alkali metals.[20-24] The high concentrations of silicon and aluminum sources necessary to achieve a sufficiently large zeolite yield generate sol gel media comprised of soluble species (monomers and oligomers) and a substantial quantity of amorphous species. It is generally believed that nucleation occurs by two-step processes, although this area of research for zeolites is not well understood. The multitude of (alumino)silicate species makes it challenging to identify a single growth unit, thereby negating the use of supersaturation as a reliable metric for predicting crystallization.[25] Moreover, growth units can potentially evolve in their speciation and concentration throughout zeolite synthesis,[26-29] which allows for multiple crystallization pathways to occur simultaneously (e.g. both classical and nonclassical mechanisms).[30, 4]

In this study we begin by reviewing recent literature from our group and others examining the assembly and role of precursors in zeolite crystallization, with an emphasis on the diverse properties of amorphous species. Recent work from our group has shown that the manipulation of amorphous particle properties, such as the distribution of alkali metals, or the ability to control the colloidal stability of precursors are two approaches to markedly impact the rate of crystallization. In order to assess the broader applicability of these two approaches, we conduct a series of experiments for zeolites with diverse properties (structure and composition) prepared by different methods involving inorganic and organic structure-directing agents.

2. Zeolite Crystallization Mechanisms

There is ample evidence for zeolite growth by classical monomer addition (Fig. 1A).[31, 32] Ex situ atomic force microscopy (AFM) images by Anderson and coworkers of numerous zeolite crystals extracted at the end of syntheses reveal layers with step heights equivalent to unit cell dimension(s),[33, 34] suggestive of a layer-by-layer growth mechanism. In situ AFM imaging of zeolite A (LTA type) at low supersaturation has provided direct evidence of layer generation and spreading.[31] These collective examples indicate the classical pathway is predominant at later stages of zeolite synthesis where supersaturation is low and amorphous precursors have largely been consumed. At higher supersaturation, but still in the absence of amorphous precursors, in situ AFM measurements of zeolite A surface growth have captured evidence of two distinct nonclassical growth pathways.[35] The first is (nearly) oriented attachment of nanocrystallites

(Fig. 1B,C) where the faceted crystal deposit (Fig. 1C, inset) continues to grow post-attachment. A second pathway is the formation of gel-like islands (Fig. 1F,G) in growth media devoid of any particulates (i.e. so-called clear solutions). Recently, dissolution experiments have been used to extract information of zeolite crystallization at early stages using NH_4F as an etchant to indiscriminately dissolve Al-O and Si-O bonds in zeolite crystals.[36] Analysis of silicalite-1 (MFI type) by this approach showed that dissolution preferentially occurs at the center of coffin-shaped crystals where nonclassical pathways presumably lead to more defects (Fig. 1D) compared to the exterior rim of crystals, which grow by a classical pathway leading to fewer defects. Examination of partially dissolved zeolite MFI crystals by AFM revealed clusters of spheroidal crystals (Fig. 1E), which were confirmed by transmission electron microscopy (TEM) to be arranged in crystallographic registry.[37] These images provide evidence of colloidal assembly at early stages of growth (i.e. interior of the crystal) where ripening at later synthesis times obscures evidence of this nonclassical pathway – analogous to phenomena observed for other minerals, such as magnetite.[38, 39]
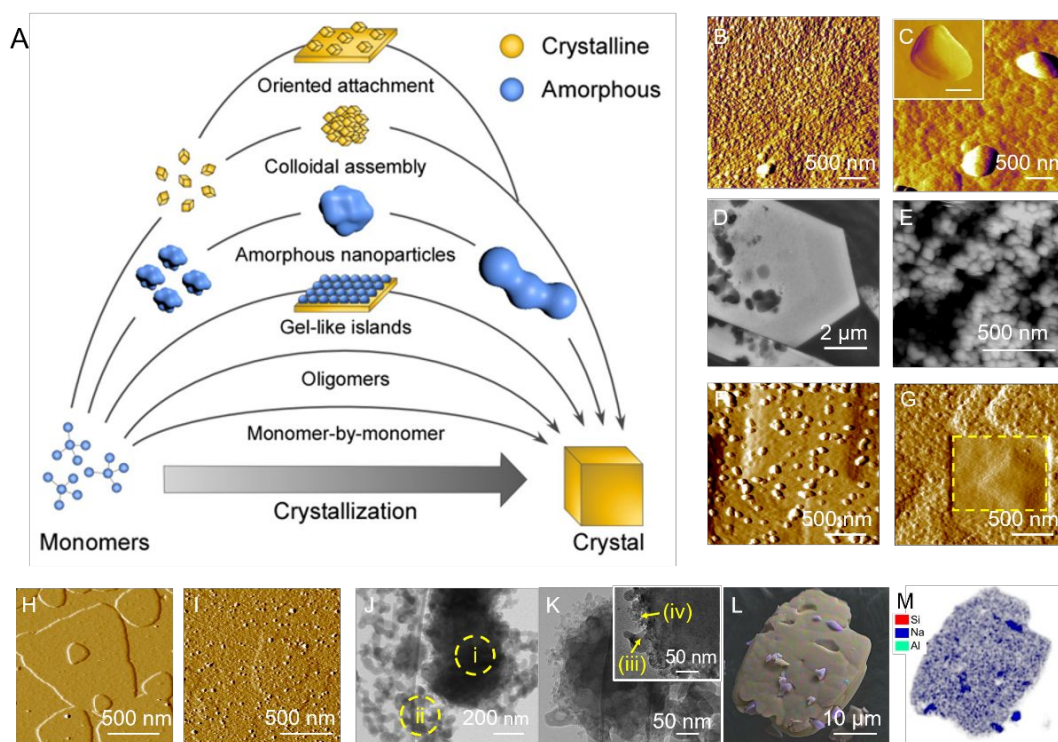
Fig. 1. (A) Illustration of crystallization pathways observed in zeolite synthesis involving amorphous (blue) and crystalline (gold) precursors. (B,C) *In situ* AFM images of zeolite A after (B) 60 min and (C) 312 min of growth at 45 °C by (nearly) oriented attachment.[35] Inset: nanocrystal marked with the arrow. Scale bar equals 500 nm. (D) SEM image and (E) AFM image of a partially dissolved ZSM-5 crystal in NH_4F revealing evidence of colloidal assembly.[37] (F) *In situ* AFM images of a zeolite A surface growth at 35 °C showing gel like islands.[35] (G) Enlarged scan size of panel F showing an area (dashed line) after continuous imaging in tapping mode. (H – M) Evidence of growth by amorphous nanoparticle attachment. (H,I) *In situ* AFM images of silicalite-1 surface growth after (H) 0 min and (I) 60 min of growth at 60 °C showing the attachment of amorphous precursors.[26] (J) TEM image of SSZ-13 solids extracted once Bragg peaks are detected in powder XRD patterns showing populations of (i) amorphous precursors and (ii) SSZ-13 crystals.[30] (K) High resolution image of a crystal in panel J showing (iii) precursor attachment and (iv) smaller (unknown) particulates surrounding crystals that are putative intermediates of the disorder-to-order transition. (L,M) FE-SEM-EDX mapping of a mordenite crystal extracted near the end of crystallization where high density of Na^+ ions (blue) is associated with residual amorphous particles.[40] All images are published with permission from the cited references.

At higher (alumino)silicate concentrations representative of most zeolite syntheses, growth mixtures are sol gels comprised of both amorphous precursors and soluble species (monomer and oligomers).[41] Several studies of different zeolite crystal structures have shown evidence of crystallization by particle attachment (CPA). In situ AFM measurements of silicalite-1 (MFI) growth reveal complete coverage of surfaces with amorphous precursors (Fig. 1H,I) where layers advance by simultaneous processes of CPA and monomer addition.[26] TEM images of solids extracted from a SSZ-13 (CHA type) synthesis at the point where the first Bragg peaks are detected in powder X-ray diffraction (XRD) patterns reveal a mixture of amorphous precursors (Fig. 1J, *i*) and rough spheroidal crystals (Fig. 1J, *ii*).[30] High resolution images of these crystals show amorphous precursors attached to the surface (Fig. 1K, *iii*) as well as smaller particulates of unknown structure (Fig. 1K, *iv*) that are putative intermediates during the disorder-to-order transition of CPA. Time-resolved studies of mordenite (MOR type) crystallization by field emission scanning electron microscopy with energy dispersive X-ray spectroscopy (FE-SEM-EDX) show remnants of undissolved amorphous precursors (regions of higher Na^+ density in Fig. 1L,M) at the end of crystallization when powder XRD seemingly indicates synthesis is complete.[40] In all of these examples (Fig. 1H – M), nonclassical CPA is a prominent growth mechanism.

The complex sol gels used to prepare zeolites are derived from the mixture of silicon and aluminum sources. Most silicon sources lead to the formation of particles (Fig. 2A) with a coreshell structure comprised of siliceous cores and aluminous shells. Reagents are generally added in such high quantity that solids do not fully dissolve, and thus amorphous precursor particles persist through much of the crystallization period. The presence of Al-rich shells can impact the rate of silica dissolution (i.e. exchange between solid and solution species), whereas the selection of the silicon source can lead to particles with distinctly different microstructure. The latter was revealed from X-ray pair distribution function (PDF) analysis of three as-received reagents (Fig. 2A) showing a histogram of atom-atom distances. All sources exhibit common SiO_4 local structure and the lack of long-range order; however, sources such as fumed silica possess intermediate-scale structure (i.e. more ordered peaks). PDF profiles of the other two sources (colloidal silica and potassium silicate) contain broad, diffuse features that do not overlap beyond 4.5 Å, suggesting differences in Si–O–Si bond connectivity. These subtle differences in local microstructure can potentially impact zeolite nucleation and growth in ways that are not fully understood.

One of the most widely studied zeolites is silicalite-1 (MFI type) where syntheses commonly employ a fourth silicon source, tetraethyl orthosilicate (TEOS), which leads to the assembly of nanoparticles (1 − 6 nm)[26] with a hydrated amorphous silica core (Fig. 2B) and a shell of organic structure-directing agent, tetrapropylammonium. These particles contain water, analogous to other systems such as amorphous calcium carbonate (ACC),[42-46] phosphate (ACP),[47, 48] and oxalate (ACO)[49] that are the precursors to diverse biominerals. In zeolite syntheses, the silicon sources analyzed by PDF are more common and lead to the formation of larger particles (Fig. 2C). Over the course of hydrothermal treatment, zeolite precursors can evolve in both size and shape. The scheme in Fig. 2C and corresponding SEM images document the changes observed to precursors of zeolite L (LTL type) during the induction period where aggregation, fusing, and ripening can lead to worm-like particles.[50, 51] Prior studies have also shown that precursors can evolve in microstructure. For example, the nanoparticles in silicalite-1 syntheses (Fig. 2B) can undergo a transition to more ordered particles at a local scale, but still lacking long-range order of a zeolite crystal. We recently reported[26] that the judicious selection of organic additives can facilitate structural reordering, which in turn promotes nonclassical CPA; however, systems where the precursors preserve a more disordered state are more likely to grow by monomer addition (Fig. 2D). Thus, it is possible to tune the pathway of crystallization by controlling the microstructural evolution of amorphous precursors. It remains to be determined if similar phenomena govern crystallization pathways in other minerals. Indeed, precursor "evolution" has been reported for ACC and ACP systems where temporal changes in precursor hydration can impact nucleation and growth, with concomitant effects on polymorph selection and/or crystal habit.[2, 3, 44]
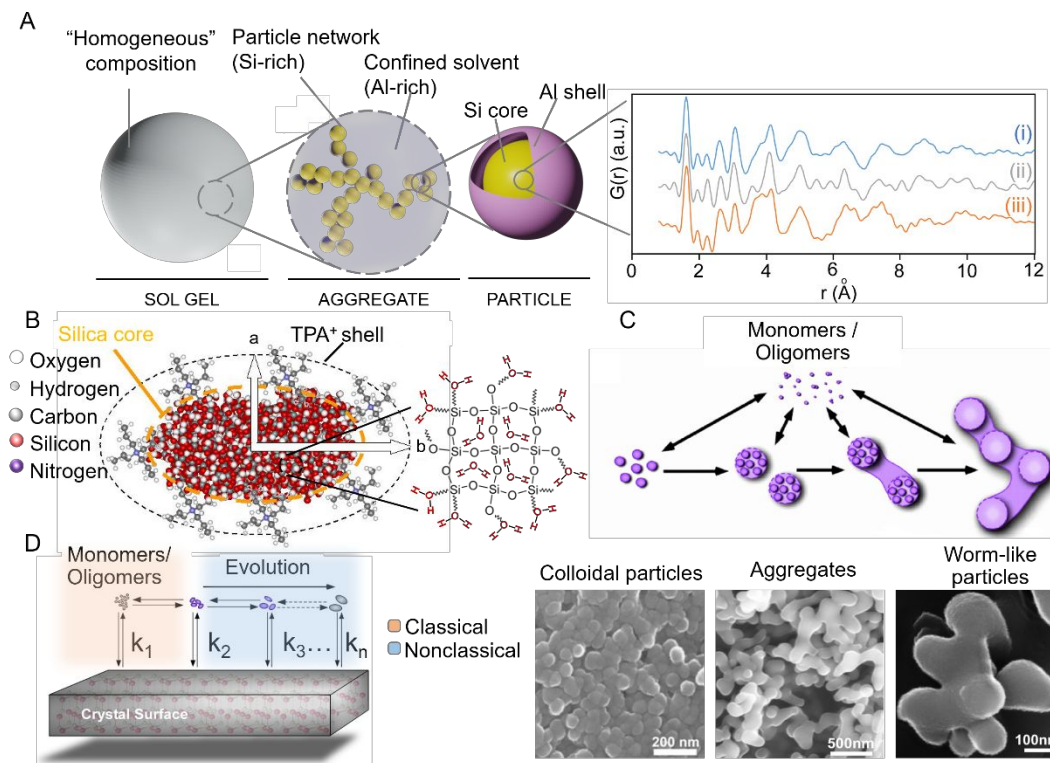
Fig. 2. (A) Complexity of sol gels from macroscopic to atomic scale (left to right). Gels are comprised of amorphous silica particles where aluminum coats the particles, which can impact their rate of dissolution. The local microstructure of silicon sources also varies, as indicated by X-ray PDF analysis (far right)[52] of three common reagents: colloidal silica (red), fumed silica (blue), and potassium silicate (black). (B) One of the most extensively characterized precursors are the nanoparticles of silicalite-1 synthesis formed by the hydrolysis of TEOS. The particles are comprised of hydrated amorphous silica (callout) with tetrapropylammonium cations used as the organic structure-directing agent forming a shell.[26] (C) Amorphous precursors can evolve in size and shape from colloidal particles to aggregates where ripening leads to the fusing of precursors and potential formation of worm-like particles. Representative scanning electron micrographs of each stage are show below the scheme for solids extracted from a zeolite L synthesis at periodic times during the induction period.[50] (D) Amorphous precursors can also evolve in microstructure, as illustrated for the nanoparticles in panel B where hydrothermal treatment leads to more ordered precursors.[26] We previously showed that more ordered precursors have a greater propensity to be involved in nonclassical CPA, whereas precursors that preserve their initial, more disordered state, are bystanders, thereby allowing growth to predominantly occur by monomer addition. All images are published with permission from the cited references.

3. Methods to Enhance the Rate of Zeolite Crystallization

Prior studies of zeolite L (LTL) crystallization have shown that the selection of silicon source can have a notable impact on the induction time.[50] In a recent study[53] we observed zeolite L nucleation within 8 – 10 h (Fig. 3A) using either colloidal or fumed silica; however, substitution of these sources with potassium silicate reduced the induction time nearly five-fold. Our hypothesis for more rapid nucleation was the spatial distribution of potassium cations within the interior of amorphous silicate particles. Elemental mapping of samples prepared from as-received reagent (Fig. 3B) revealed K^+ ions distributed throughout the amorphous silica particles. The presence of alkali metal in the synthesis medium is critical since K^+ ions function as

inorganic structure-directing agents to facilitate the formation of pores in the LTL crystal structure. The infusion of precursors with alkali (Fig. 3C) was deemed significant to promote zeolite nucleation, which putatively occurs either on the surface or within the interior of amorphous precursors. The potential pathways of zeolite nucleation in complex sol gel media are diverse and generally not well understood, but the ability to alter precursor composition with respect to the inorganic structure-directing agent is seemingly influential. To test this effect, a modified fumed silica was prepared by incubating the silicon source in $KBr_{(aq)}$ solution for one week to infuse K^+ within amorphous particles, which was confirmed by elemental analysis.[53] Zeolite L syntheses using the modified fumed silica resulted in similar induction time as potassium silicate (Fig. 3A). In a broader context, the infusion of amorphous precursors with metals has implications for many crystalline materials. For example, nearly all natural zeolites are comprised of alkali and/or alkaline earth metals.[54, 13, 55] In biomineralization, metals are also prevalent and can function as crystal growth modifiers.[56-58] This was recently demonstrated in calcium carbonate by De Yoreo and coworkers[59] who showed that ACC infused with Mg^{2+} ions modifies precursor hydration and inhibits its evolution, which impacts the kinetics of $CaCO_3$ crystallization and crystal size.
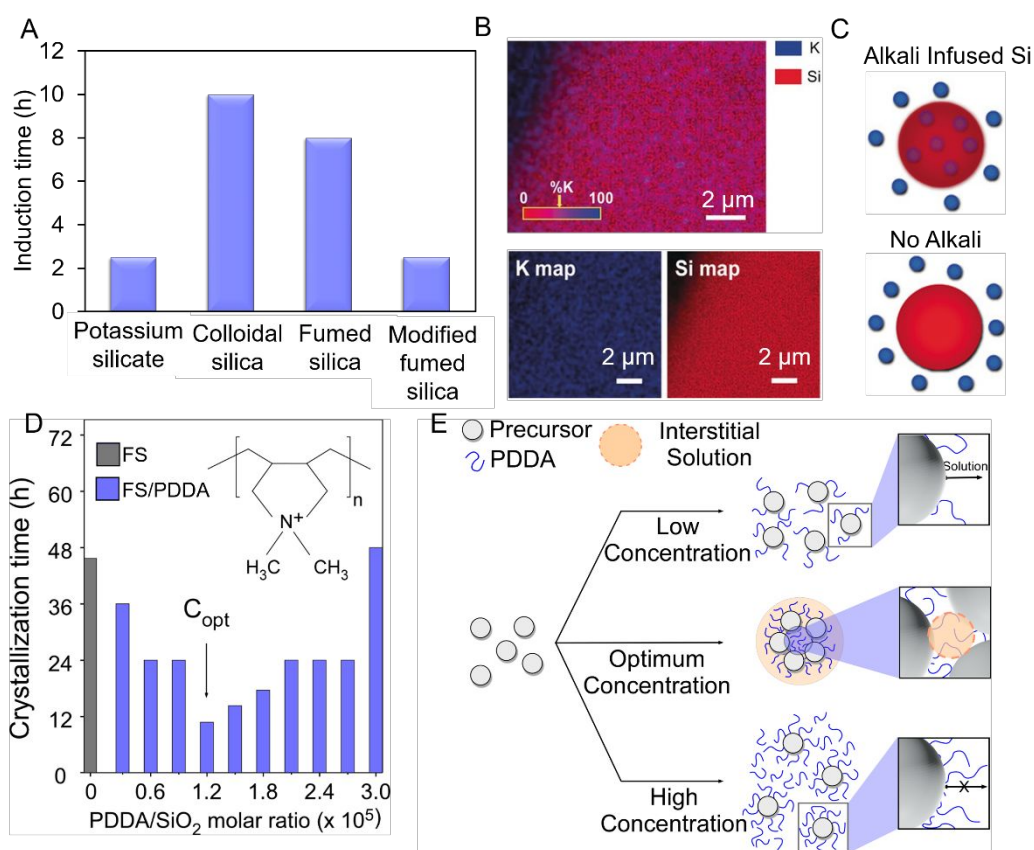
Fig. 3. (A) Induction time of zeolite L (LTL) syntheses with three as-received silicon sources (potassium silicate, fumed silica, and colloidal silica) and a modified fumed silica incubated in 2 M $KBr_{(aq)}$ solution at room temperature for 7 days.[53] Times are estimated from the first appearance of Bragg peaks in powder XRD patterns. (B) FE-SEM-EDX elemental mapping of modified fumed silica showing K^+ ions (blue) evenly distributed throughout the particle.[53] (C) Idealized scheme of alkali-infused amorphous silica particles (e.g. potassium silicate and modified fumed silica) and particles without alkali infusion (e.g. fumed and colloidal silica). (D) Crystallization time of SSZ-13 in the absence (grey) and in the presence (blue) of PDDA at increasing polymer concentration (or PDDA/SiO_2 molar ratio).[60] The shortest crystallization time occurs at an optimal PDDA concentration (C_{opt}) around 0.2 wt% polymer. (E) Cartoons illustrating how increased coverage of polymer on amorphous precursors with increasing polymer concentration putatively

impacts precursor – solution exchange, precursor aggregation, and the generation of confined interstitial pockets of solution between aggregated precursors at C_{opt}.[60] All images are published with permission from the cited references. Unpublished data from panels D and E are included as Supporting Information.

Among the examples discussed, it is evident that the physicochemical properties of amorphous precursors, such as microstructure or composition, can impact growth pathways and the kinetics of zeolite crystallization; however, we recently observed that the colloidal stability of precursor particles is another factor that can be manipulated in ways that markedly accelerate the rate of zeolite crystallization, analogous to the effects of alkali-infused precursors. The impact of colloidal stability was tested on syntheses of zeolite SSZ-13 (CHA type) using sol gels prepared with fumed silica and N,N,N-trimethyl-1-1-adamantammonium (TMAda) as an organic structure-directing agent.[61, 62] Addition of the polymer polydiallyldimethylammonium (PDDA) to the synthesis medium resulted in a non-monotonic trend (Fig. 3D) where low quantities of PDDA lead to a reduction in SSZ-13 crystallization time with increased polymer concentration until reaching an optimal concentration (C_{opt}), above which further increase in polymer concentration results in longer crystallization times. Interestingly, similar trends were not observed with other polyamines, which may be attributed to the fact that PDDA is comprised of quaternary amines, similar to the structure-directing agent TMAda. Our hypothesis for this trend in crystallization kinetics is outlined in Fig. 3E where low and high PDDA concentrations result in low and high coverage of polymer on the surfaces of amorphous precursors that do not induce colloidal aggregation. We posit that low PDDA coverage does not significantly obstruct the exchange of (alumino)silicate species between precursors and solution, but does inhibit Ostwald ripening. The latter effect preserves the smaller size of precursors (i.e. higher surface area), which putatively enhances zeolite nucleation. Small particle size is also preserved at high PDDA coverage; however, it is likely that these conditions adversely impact the exchange of species between solid and solution states, thus leading to longer crystallization times. At C_{opt} it was observed by multiple light scattering techniques that PDDA promotes the aggregation of precursors. We proposed a hypothesis that the solution within interstitial spaces of aggregated precursors promotes nucleation. It is likely that higher local supersaturation can be generated in these confined pockets of solution via the dissolution of (alumino)silicate species. The presence of PDDA within these interstitial regions may also be critical. For instance, we found that the optimal concentration of PDDA can facilitate the condensation of free silicate monomer (or oligomers) in solution, which could lead to the formation of clusters to promote nucleation by a two-step mechanism.

Herein, we examine the generalizability of the two phenomena outlined in Fig. 3. We first go beyond zeolite L to determine if alkali-infused precursors can accelerate the rate of crystallization for other zeolites. We then examine if PDDA addition to diverse zeolite synthesis mixtures can have the same impact on crystallization time as was observed for zeolite SSZ-13. To perform these experiments, we selected three commercially relevant zeolites with different crystal structures: SSZ-13 (CHA, small pores), ZSM-5 (MFI, medium pores), and mordenite (MOR, large pores). The choice of structures targeted materials formed under synthesis conditions in the presence or absence of organics and disparate alkali metals (e.g. potassium and sodium). We also assessed whether the combination of both approaches, polymer addition to mixtures with metal infused precursors, could lead to synergistic outcomes in zeolite crystallization.

4. Experimental Methods

4.1 Materials. The following chemicals were purchased from Sigma Aldrich: Sodium aluminate (technical grade), sodium hydroxide (NaOH, 98%), fumed silica (SiO_2, 99.8%), colloidal silica (SiO_2, 40% in water), aluminum hydroxide (76.5 wt % $Al(OH)_3$, reagent grade), and polydiallyldimethylammonium chloride (PDDAC, MW = 150k, 20 wt % in H_2O). Tetrapropylammonium hydroxide (TPAOH, 40% in H_2O) and N,N,N-trimethyl-1-1-adamantammonium hydroxide (TMAdaOH, 25 wt % in H_2O) were purchased from

Alfa Aesar and SACHEM Inc., respectively. Sodium hydroxide (NaOH, 1M) was procured from Supelco, while sodium bromide (NaBr, 99.7%) was purchased from J.T. Baker. Deionized (DI) water was produced with an Aqua Solutions RODI-C-12A purification system (18.2 MΩ). All reagents were used as received without further purification.

4.2 Preparation of zeolites. The generation of modified fumed silica using sodium as the alkali metal was performed according to a previously reported procedure[53] wherein as-received fumed silica was incubated in 2M NaBr solution (10g fumed silica in 200g of 2M NaBr solution) at room temperature for 7 days. Modified (or sodium-infused) fumed silica was recovered by two centrifuge and wash cycles with DI water and then dried in an oven at 50 °C and ambient pressure. The same procedure was repeated using pure DI water (10g fumed silica in 200g of water) in place of 2M NaBr for an identical incubation time. The resulting water-treated fumed silica was isolated by the same centrifuge/washing procedure.

Synthesis of zeolite SSZ-13 (CHA) was performed according to a reported protocol[30] using TMAda as the organic structure-directing agent. In a typical synthesis, sodium hydroxide solution (50 wt%, 0.18g, 0.0023 mol) and TMAdaOH (0.95g, 0.0011 mol) were first mixed with DI water (8.13g, 0.4960 mol), and stirred for 15 min at room temperature. Aluminum hydroxide (0.06g, 0.0006 mol) was then added to the mixture, which was stirred for an additional 15 min. To this mixture was added fumed silica (0.68g. 0.0113 mol) to produce a final molar composition of $0.052\ Al(OH)_3$: $1.0\ SiO_2$: $0.2\ NaOH$: $44\ H_2O$: $0.1\ TMAda$. The growth mixture was aged at room temperature for 4 h under continuous stirring and then transferred to a 23-ml Teflon-lined stainless steel acid digestion bomb (Parr Instruments). The sealed autoclave was heated in a Thermo Scientific Precision oven under rotation (30 rpm) and autogenous pressure at 180 °C for different synthesis times.

Synthesis of zeolite mordenite (MOR) was performed according to a reported protocol[63] using an organic-free recipe with sodium as the inorganic structure-directing agent. In brief, sodium hydroxide (98%, 0.54g, 0.019 mol) was dissolved in DI water (25.92g, 1.428 mol), followed by the addition of sodium aluminate (0.50g, 0.003 mol) with continuous stirring for 15 min. To this mixture was added fumed silica (3.03 g, 0.050 mol) and the resulting sol gel was aged overnight at room temperature under continuous stirring. The aged solution was then transferred to a Teflon-lined acid digestion bomb and place in an oven at 165 °C under rotation for different synthesis times.

Synthesis of zeolite ZSM-5 (MFI) was performed according to a reported protocol[64] using tetrapropylammonium (TPA) as an organic structure-directing agent. First, NaOH (1M, 2.39g, 0.0023 mol) and TPAOH (0.8624g, 0.0017 mol) were dissolved in DI water (10.34g, 0.574 mol). To this mixture was added sodium aluminate (0.0827g, 0.0011 mol) with continuous stirring for 15 min; and then the silicon source (1.02 g, 0.017 mol) was added to the solution. The growth solution was aged for 2 h at room temperature and transferred into an acid digestion bomb. Unless otherwise stated, ZSM-5 was synthesized at 180 °C under static conditions for different times. For all zeolite syntheses, solids were extracted by removal of acid digestion bombs from the oven and cooling in a water bath to room temperature. The samples were subjected to the same centrifuge and washing procedure until neutral pH was achieved.

For studies of modified fumed silica, the silicon source in the above recipes was replaced by either alkali-infused or water treated sources (86 wt% SiO_2). For the former, additional quantities of Na and Br in the modified silicon source were not accounted in the molar composition of the recipe. For syntheses involving the addition of PDDA, the above recipes were altered by adding polymer prior to the addition of aluminum and silicon sources. The $PDDA/SiO_2$ molar ratio used for each zeolite growth mixture was selected by screening syntheses for the optimal composition leading to the fastest crystallization time. Syntheses of mordenite and SSZ-13 with colloidal silica was done following the same protocol as mentioned above where fumed silica was replaced with colloidal silica while keeping the molar compositions the same.

4.3 Materials characterization. As-synthesized materials were characterized for their crystallinity and phase purity by powder X-ray diffraction (XRD) on a Rigaku diffractometer (Cu Kα radiation). Analysis of bulk elemental composition was performed using energy dispersive X-ray spectroscopy (EDX) on a JEOL SM-31010/METEK EDAX system. The morphology of zeolite crystals was determined by scanning electron microscopy (SEM) using a FEI 235 dual-beam (focused ion-beam) system. The aggregation of silica particles was studied by dynamic light scattering using Brookhaven Instruments BI-200SM machine equipped with a TurboCorr Digital Correlator, a red HeNe laser diode (35 mW, 637 nm), and a decalin bath that was filtered to remove dust. The composition of the solutions used for DLS experiments was based on a reported protocol[65] using a dilute, aluminum-free solution to mimic zeolite synthesis conditions (molar composition of 1 SiO_2 : 1 NaOH : 350 H_2O). DLS experiments were conducted at a fixed scattering angle of 90 °, and the autocorrelation function was collected over a 1-min timeframe with at least 5 measurements for each sample.

Oblique illumination microscopy (OIM) measurements were performed using to assess PDDA-induced aggregation of silica precursors using a Nanosight LM10-HS microscope (Nanosight Ltd) equipped with a green laser (λ = 532 nm) operating at 25 ± 0.1 °C. OIM measures the Brownian motion of individual particles (or clusters). The composition of solutions prepared for OIM experiments was based on a reported protocol[60] using a molar composition of 1 SiO_2: 1 NaOH: 1760 H_2O: 0.1 TPAOH. Textural analysis of different silicon sources was performed by by N_2 adsorption/desorption using a Micromeritics ASAP 2020 instrument. For all zeolite syntheses, the pH of the growth medium (or extracted supernatant solution) was measured using a Thermo Scientific Orion 3 Star meter.

5. Results and Discussion

5.1 Alkali-infused precursors as crystallization accelerants. Here we assess the broader applicability of alkali-infused silicon sources to reduce the time of zeolite crystallization for the synthesis of zeolite mordenite (MOR). Crystallization was carried out in an organic-free medium using Na^+ as the structure-directing agent,[63] and an alkaline sol gel mixture (pH 12 – 13) prepared with fumed silica (sample FS) as the silicon source. Time-resolved powder XRD patterns of solids extracted from growth mixtures at various heating times reveal nucleation within 24 h and a fully crystalline product after ca. 36 h (Fig. 4A). The same experiments was then performed using a modified fumed silica that was pre-treated in a sodium bromide solution for one week. Elemental analysis of the extracted solid powder was performed by energy dispersive X-ray spectroscopy (EDS) to confirm the occlusion of alkali in modified amorphous silica (Table S1). The resulting sodium-infused fumed silica (sample FS-a) was used to prepare a mordenite growth mixture with the same composition as the control. Time-resolved powder XRD patterns of solids extracted from syntheses with FS-a (Fig. 4B) resulted in a marked reduction in both induction time (< 8 h) and crystallization time (ca. 16 h). We also conducted an experiment where additional NaBr was added to the growth mixture to assess the effects of excess Na^+ in FS-a and whether pre-treatment was necessary for alkali infusion. Our findings showed that the synthesis using FS as the source and the addition of NaBr (equivalent to quantity in FS-a) resulted in a crystallization time (Fig. S1A) comparable to FS-a, suggesting the effect of alkali occurs *in situ* without the need for pre-treatment. To assess whether alkali in solution impacts mordenite crystallization, we replaced FS with colloidal silica (a nonporous precursor). Additional NaBr in synthesis mixtures reduced the crystallization time (Fig. S1B), indicating that a higher concentration of Na^+ ions in the growth medium, present either in the solid or solution, impact the rates of mordenite crystallization.

The evolution of amorphous precursors from both FS and FS-a sources was evaluated using DLS to measure changes in the hydrodynamic diameter of silicate particles with heating time. In order to prepare solutions with the appropriate volume fraction of dispersed silica particles for scattering experiments, we adapted a previously established protocol[65] wherein a dilute zeolite synthesis mixture is prepared without the addition

of alumina to avoid coagulation. Over a 24-h period of hydrothermal treatment, we observe a monotonic increase in amorphous particle size for sample FS (Fig. 5A and Fig. S2A). Conversely, the particle size of the alkali-treated sample FS-a exhibits a step change increase with initial heating, followed by a more pronounced monotonic increase in size with time (Figs. 5A and S2B). The exact cause for modified fumed silica reducing mordenite synthesis time is not fully understood. In addition to the effect of alkali infusion in amorphous silica particles, similar to those observed for K^+ in zeolite L (Fig. 3A), there could be contributing factors due to particle aggregation, akin to the effects observed for PDDA in SSZ-13 synthesis (Fig. 3D). To differentiate these two potential effects we altered the pre-treatment of fumed silica by removing NaBr and using pure DI water for an equal amount of time. When the extracted powder (sample FS-w) was used as the silicon source for a mordenite synthesis (Fig. S3), we observed a crystallization time (ca. 16 h) similar to that of FS-a, but with a slightly longer induction time (< 16 h). This seems to suggest that changes to the properties of fumed silica during pre-treatment, irrespective of alkali infusion, is responsible for the altered kinetics of mordenite crystallization.
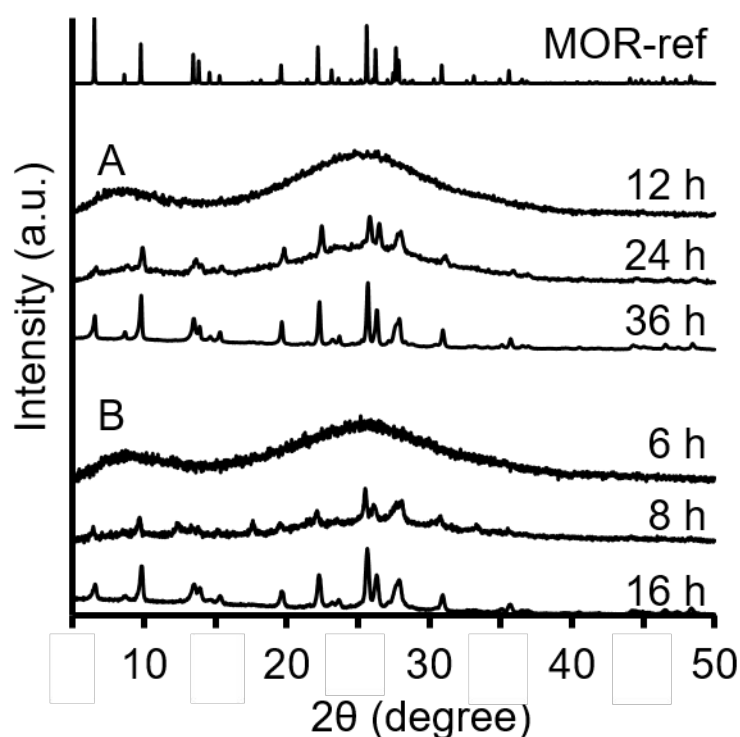
Fig. 4. Time-elapsed powder XRD patterns of solids extracted from a mordenite synthesis at various times of hydrothermal treatment at 165 °C using a molar composition of 18 SiO_2: 1 Al_2O_3: 6.8 NaOH: 509.3 H_2O. Comparisons are made between syntheses employing two different silicon sources: (A) fumed silica (sample FS) and (B) fumed silica infused with sodium ions (sample FS-a). Syntheses were performed using growth mixtures of identical molar composition, with the exception of excess NaBr in the modified fumed silica (15% NaBr by weight).

One property that is affected by pre-treatment is the porosity of fumed silica. Textural analysis of as-received fumed silica (FS) confirms the presence of micopores (Fig. 5B). If we consider amorphous silica spheres of 150 nm in average diameter (equivalent to FS in Fig. 5A), the estimated external surface area is 10 – 20 m^2/g. This accounts for 10% of the total BET surface area of FS (Fig. 5A), which indicates that the majority of surface area is attributed to the micropores. After pre-treatment with water (FS-w), there is a two-fold increase in micropore volume without significant loss of BET surface area. Pre-treatment with

NaBr (FS-a) leads to a reduction in micropore volume and BET surface area, presumably due to the occupancy of Na^+ and Br^- ions within the micropores of amorphous silica particles. The exact impact of micropores on mordenite crystallization remains elusive; however, there are clear differences among FS, FS-w, and FS-a in terms of precursor evolution with concomitant impact on the size and morphology of mordenite crystals. Scanning electron microscopy (SEM) images of fumed silica after a short period of hydrothermal treatment (Fig. 5C – E) reveal differences that cannot be discerned from DLS measurements. For example, sample FS-a (Fig. 5E) and sample FS-w (Fig. 5D) both resemble worm-like particles (Fig. 2C), whereas sample FS (Fig. 5C) is comprised of nanosized domains similar to the original sample prior to hydrothermal treatment. These differences among amorphous precursors translate into disparate morphologies of the final mordenite crystals, as verified by SEM (Fig. 5F – H). Notably, the crystals obtained from FS (Fig. 5F) are somewhat faceted crystals with non-uniform morphology; FS-w produces rough crystals (Fig. 5G, S3), analogous to finned zeolites reported by Dai et al.[66]; and FS-a results in more faceted crystals (Fig. 5H).
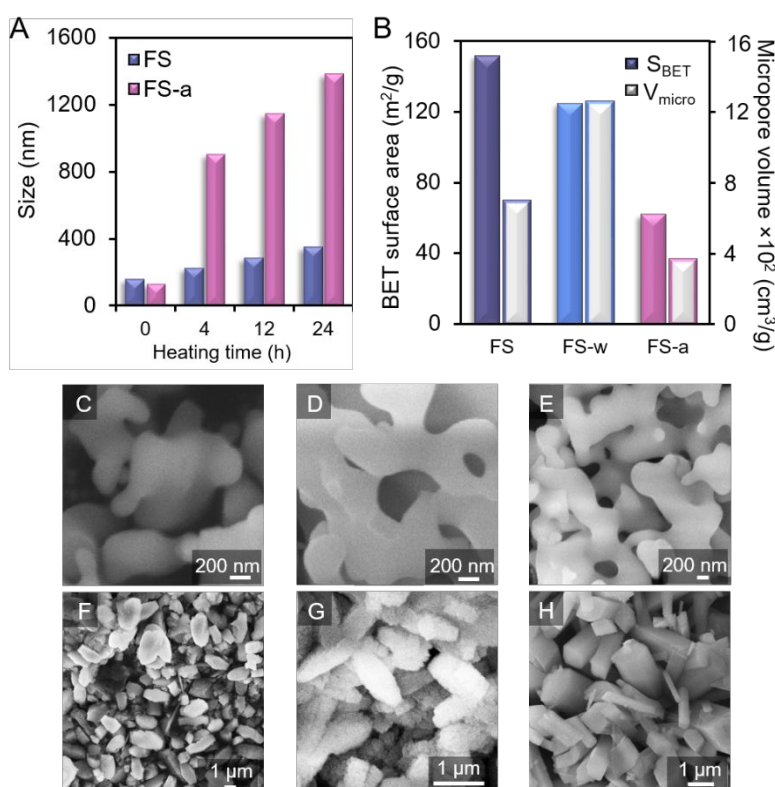
Fig. 5. (A) Dynamic light scattering measurements of amorphous precursor size as a function of hydrothermal treatment time. The heating temperature is 180 °C and the molar composition of solution prepared for DLS is 1 SiO_2: 1 NaOH: 350 H_2O (i.e. a diluted zeolite synthesis composition without the alumina source). Comparisons are made between two different silicon sources: fumed silica (sample FS) and fumed silica infused with sodium ions (sample FS-a). (B) Textural analysis of silicon sources used for all zeolite syntheses prior to hydrothermal treatment. Nitrogen adsorption/desorption measurements were used to obtain the BET surface area (left y-axis) and micropore volume (right y-axis) of amorphous precursors. (C – E) Scanning electron micrographs of amorphous precursors extracted from mordenite syntheses. The growth mixtures were prepared with three different conditions and hydrothermal treatment times: (C) FS (6 h), (D) FS-w (8 h), and (E) FS-a (6 h). (F – H) Scanning electron micrographs of fully crystalline mordenite prepared with three different silicon sources: (F) FS (36 h), (G) FS-w (16 h), and (H) FS-a (16 h).

We further assessed the impact of fumed silica pretreatment on two different zeolites prepared with organics: SSZ-13 (CHA)[30] and ZSM-5 (MFI)[64] using TMAda and TPA as structure-directing agents, respectively. Syntheses using water-treated fumed silica (FS-w, Figs. S4 and S5) did not significantly alter crystallization time compared to growth conditions using fumed silica (FS) as the silicon source (Figs. 6, S6, S7, and S8). This indicates that the enhanced rate of crystallization observed for mordenite using FS-w is not universal. A more extensive parametric study is needed to relate the effects of FS-w to factors such as growth medium composition (e.g. alkali metals, organics, etc.) and the inherent structure of the zeolite crystal. Syntheses using alkali-infused fumed silica (FS-a) resulted in consistent results for mordenite and SSZ-13, similar to those observed for zeolite L (Fig. 2A). Preparation of mordenite and SSZ-13 with the sodium-infused silicon source led to more than 50% reduction in crystallization time compared to syntheses using as received fumed silica (Figs. 6 and S6). This is unexpected for SSZ-13 given that K^+ ions (not Na^+) are the structure-directing agent used in organic-free preparation of the CHA crystal structure.[67] Conversely, Na^+ ions are used in organic-free syntheses of ZSM-5;[68] however, the substitution of FS with FS-a did not have an appreciable effect on ZSM-5 crystallization time (Fig. 6), suggesting the organic structure-directing agent plays a more important role in ZSM-5 crystallization under the conditions selected for this study.
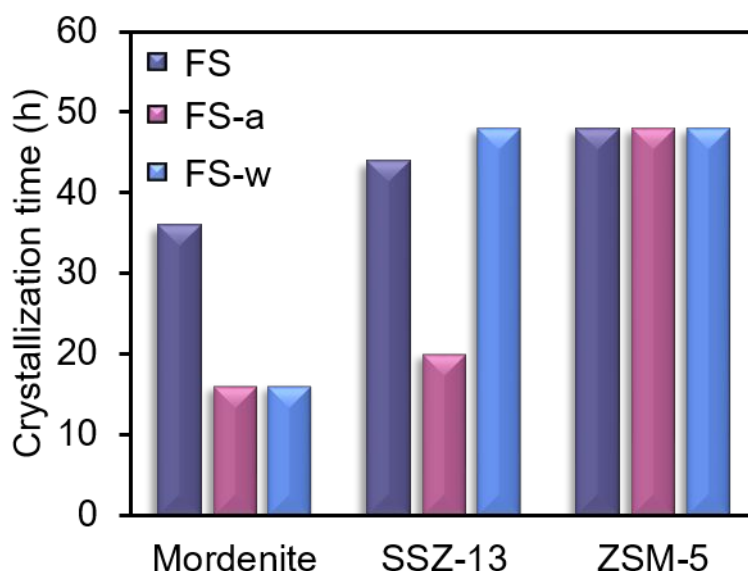
Fig. 6. Times to reach full crystallinity for syntheses of mordenite (MOR), SSZ-13 (CHA), and ZSM-5 (MFI) using FS, FS-a, and FS-w as the silicon sources. Syntheses were performed under hydrothermal conditions at temperatures of 165, 180, and 170 °C, respectively.

5.2 PDDA as a crystallization accelerant. Syntheses of mordenite and ZSM-5 using fumed silica (FS) as a silicon source were tested with the addition of PDDA polymer. Powder XRD patterns of solids extracted from syntheses at a fixed period of hydrothermal treatment and varying polymer content were compared to approximate the PDDA concentration resulting in the fastest zeolite crystallization time (Fig. S9). Syntheses in these optimal PDDA-containing growth mixtures (Fig. 7A) resulted in 2- and 3-fold reductions in crystallization time for mordenite (Fig. S10) and ZSM-5 (Fig. S11), respectively, compared to their nominal (polymer-free) syntheses. This finding is consistent with the effect of PDDA on SSZ-13 crystallization time (Figs. 3D, 7A, and S12). Likewise, the presence of PDDA inhibits the evolution of amorphous precursors into worm-like particles observed in the absence of polymer (Fig. 5C – E). SEM images of solids extracted from mordenite syntheses using FS (Fig. 7B) and FS-a (Fig. 7C) confirm that PDDA preserves the original

size of amorphous precursors. Similar observations were made for growth solutions of ZSM-5 (Fig. S11 and S13). As previously discussed (Fig. 3E), the smaller precursor size leads to higher specific surface area that enables facile exchange of (alumino)silicate species between solid and solution. In the interstitial regions of PDDA-induced aggregates, the confined volume has the potential to concentrate these species in the presence of PDDA, which has been shown to facilitate silica condensation.

We performed scattering experiments to assess whether the presence of organic structure-directing agents influenced precursor aggregation. For instance, it was previously shown for SSZ-13 that the organic structure-directing agent TMAda did not impact the ability of PDDA to induce precursor aggregation at the optimal polymer concentration. In this study, we conducted oblique illumination microscopy (OIM) measurements of solutions mimicking ZSM-5 synthesis and confirmed that its organic structure-directing agent, TPA, did not inhibit precursor aggregation in PDDA-containing solutions (Fig. S14). These studies were not performed for mordenite since its synthesis is carried out in organic-free media.
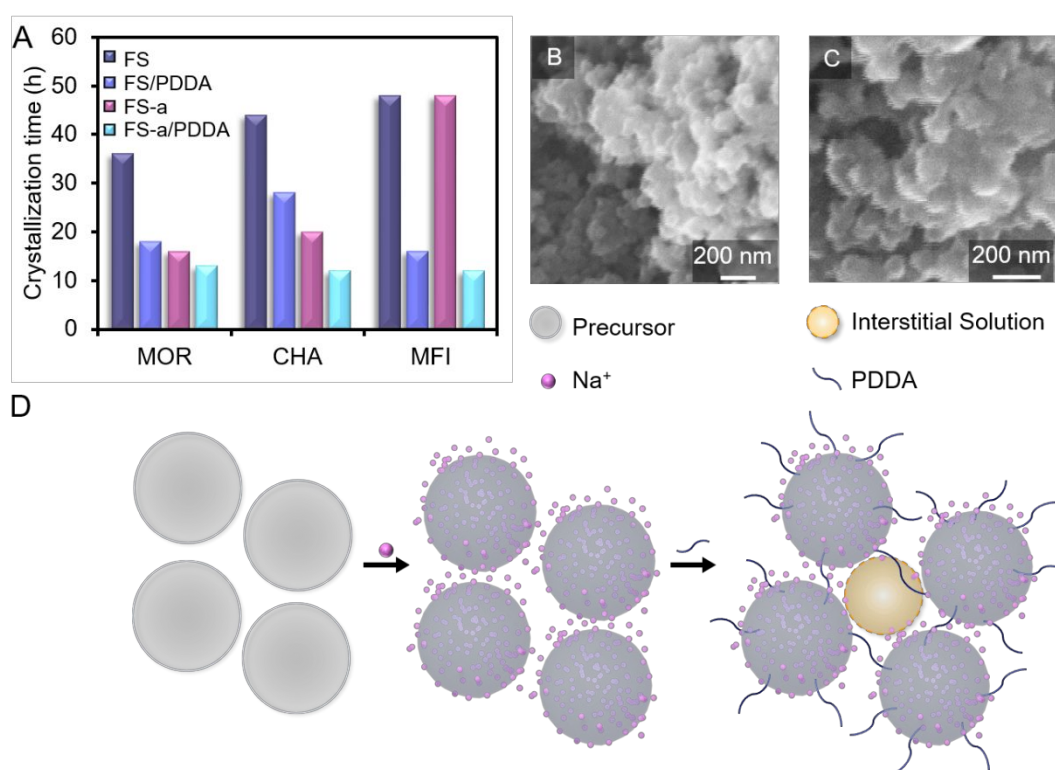
Fig. 7. (A) Times to reach full crystallinity for syntheses of mordenite (MOR), SSZ-13 (CHA), and ZSM-5 (MFI) using four conditions: FS, FS/PDDA, FS-a, and FS-a/PDDA. Data for FS and FS-a are taken from Fig. 6. The PDDA:SiO$_2$ molar ratios for MOR (6.0×10^{-6}) and MFI (2.4×10^{-5}) were determined by pre-screening for the optimal PDDA concentration (Fig. S9). The molar ratio used for CHA (1.2×10^{-5}) was set equal to C_{opt} in Fig. 3D; however, experiments by Dai et al.[60] used fumed silica from a different vendor than the source used in this study, which accounts for differences in crystallization times. (B and C) High magnification scanning electron micrograph of amorphous precursor extracted from a mordenite synthesis after 8 h of hydrothermal treatment using (B) FS/PDDA and (C) FS-a/PDDA combinations. (D) Cartoon illustrating the infusion of silicon source (fumed silica) with alkali ions during pre-treatment in 2 M NaBr$_{(aq)}$, followed by PDDA-mediated assembly of precursors into clusters at an optimal PDDA:SiO$_2$ molar ratio.

5.2 Synergistic effects of precursor modification. To assess the potential synergy between PDDA and alkali-infused fumed silica (FS-a), we also performed experiments where FS was replaced with FS-a using the same PDDA concentrations. Our findings revealed that the combination of both modifications (Fig. 7A) resulted in further reductions of crystallization time for mordenite and SSZ-13, beyond what was achieved with each individual precursor modification (Figs. S15 and S16). This confirms the synergetic effect of altering both the composition and colloidal stability of precursors in zeolite crystallization. This is roughly illustrated in Fig. 7D where we posit the interstitial confined region (shaded yellow area) is a potential site for zeolite nucleation in syntheses involving the combined use of FS-a as the silicon source and PDDA as a polymer additive. It was shown in Fig. 4A that the presence of alkali metal within amorphous precursors (FS-a) promotes particle aggregation, similar to the effect of PDDA. When FS-a and PDDA are combined, it is likely that the presence of both Na^+ ions and PDDA in the confined interstitial solution among precursor aggregates leads to the observed synergistic enhancement of zeolite nucleation for mordenite and SSZ-13; however, this effect was not observed for ZSM-5 wherein PDDA-containing solutions with and without FS-a exhibited similar crystallization time (Figs. 7A and S13).
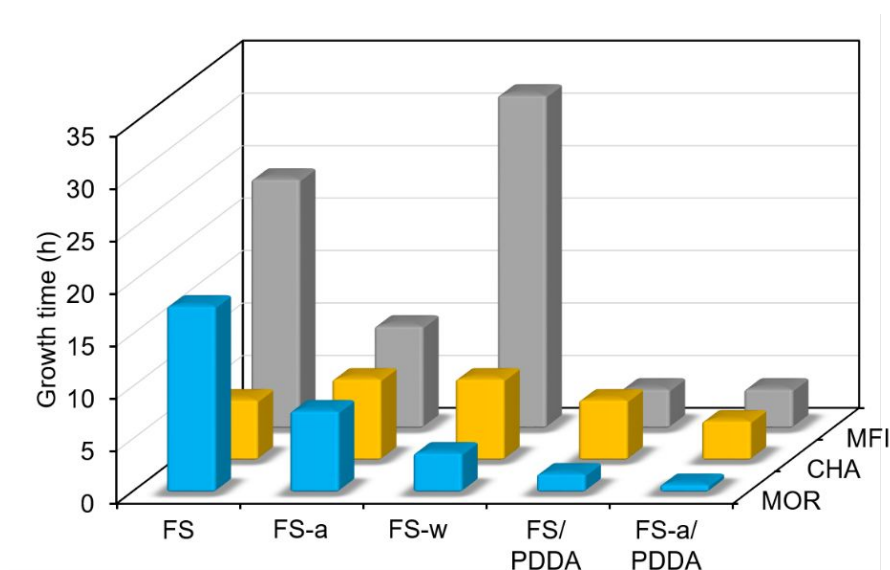
Fig. 8. Three dimensional plot of zeolite crystal growth times for all three structures (MOR, CHA, MFI) for the five synthesis conditions tested: FS, FS-a, FS-w, FS/PDDA, and FS-a/PDDA. The growth times listed here are obtained from powder XRD patterns of solids extracted at periodic synthesis times wherein the estimated induction time (i.e. first appearance of Bragg peaks in powder XRD) is subtracted from the approximate crystallization time (i.e. fully crystalline powder XRD).

We analyzed the effect that each precursor modification has on the times of nucleation and growth for the three zeolite structures tested in this study. These times were approximated from powder XRD patterns extracted at periodic synthesis times. The induction time was estimated as the first appearance of Bragg peaks, with values for each synthesis condition reported in Fig. S17. The difference between the total crystallization time (Figs. 6 and 7A) and the induction time (Fig. S17) was used to determine the time of growth (Fig. 8). For SSZ-13 the effects of alkali infusion and PDDA both had larger impact on induction time. The same trend was observed for ZSM-5 in the presence of PDDA. For mordenite the opposite trend was observed wherein alkali infusion and PDDA had more pronounced effects on the time of growth (Fig. 8). For mordenite syntheses, each modification to the synthesis mixture resulted in reduced growth time, with the synergistic combination FS-a/PDDA resulting in an 18-fold reduction relative to the control (FS). For SSZ-13 syntheses, the growth time is not significantly impacted by any of the precursor modifications, indicating that the reduced crystallization time is attributed to accelerated nucleation. For ZSM-5 syntheses,

the only reductions in total crystallization time were observed for PDDA-containing solutions where reductions in the times of nucleation (Fig. S17) and growth (Fig. 8) relative to those of the control were observed. Collectively, our findings reveal that precursor modifications can have notable impacts on nucleation and/or growth times with trends among zeolites that not predictable.

6. Conclusions

The amorphous-to-crystalline transformations observed in this study for zeolite syntheses are common to many other systems where the impact of physicochemical properties of amorphous precursors on processes of crystal nucleation and growth is often elusive. In this study, we tested a small sampling of zeolites among the approximately 250 known structures; thus, it is uncertain if the trends observed in this study are broadly applicable to structures beyond the three investigated (MOR, CHA, and MFI). Here we examined the effects that two modifications to amorphous precursors had on zeolite crystallization, focusing on syntheses using fumed silica as the sole silicon source. Our findings revealed that colloidal stability impacts all three zeolites wherein the addition of a polymer additive, PDDA, can induce precursor aggregation with concomitant reductions in crystallization time. A working hypothesis was presented where we posit the interstitial (confined) regions between aggregated precursors leads to enhanced rates of crystallization, coupled with the presence of PDDA that can facilitate silicate condensation (potentially enhancing the rate of nucleation).

Alkali infusion had a pronounced impact on SSZ-13 and mordenite, while ZSM-5 was the only zeolite tested that was unaffected by the addition of Na^+ ions. It remains to be determined if the reduced crystallization time for mordenite using the FS-a modified silicon source is a general outcome for organic-free syntheses. Likewise, it is uncertain if ZSM-5 crystallization being unresponsive to substitution of FS with FS-a represents an anomaly among zeolite syntheses using organic structure-directing agents. Future investigations that expand this work to other zeolites can potentially shed more light on the impact of precursor modifications. It is evident, though, that these facile changes to amorphous precursors could be easily implemented in industrial syntheses. The ability to reduce crystallization times by the extent demonstrated in this study could have significant impact on the economics of commercial production. Moreover, the concept of alkali infusion could have potential parallels with heteroatom insertion in zeotypes. It is too premature to make these comparisons; however, similar concepts have been validated for interzeolite transformations where ion exchange of a parent zeolite (seed) with metals has been used to generate daughter zeolites (product) with occluded metals.[69, 70] It remains to be determined if similar outcomes can be emulated in amorphous precursors to impact the crystallization pathways and resultant physicochemical properties of zeolites, zeotypes, and related materials that occur by nonclassical pathways.

References
1.　J. Baumgartner, A. Dey, P. H. Bomans, C. Le Coadou, P. Fratzl, N. A. Sommerdijk and D. Faivre, *Nat. Mater.*, 2013, **12**, 310-314.
2.　E. Beniash, R. A. Metzler, R. S. Lam and P. Gilbert, *J. Struc. Biol.*, 2009, **166**, 133-143.
3.　Y. U. Gong, C. E. Killian, I. C. Olson, N. P. Appathurai, A. L. Amasino, M. C. Martin, L. J. Holt, F. H. Wilt and P. Gilbert, *PNAS*, 2012, **109**, 6088-6093.
4.　A. I. Lupulescu and J. D. Rimer, *Science*, 2014, **344**, 729-732.
5.　Y. Politi, T. Arad, E. Klein, S. Weiner and L. Addadi, *Science*, 2004, **306**, 1161-1164.

6.   P. R. ten Wolde and D. Frenkel, *Science*, 1997, **277**, 1975-1978.

7.   L. F. Filobelo, O. Galkin and P. G. Vekilov, *J. Chem. Phys.*, 2005, **123**, 014904.

8.   P. G. Vekilov, *Cryst. Growth Des.*, 2010, **10**, 5007-5019.

9.   T. Yamazaki, Y. Kimura, P. G. Vekilov, E. Furukawa, M. Shirai, H. Matsumoto, A. E. Van Driessche and K. Tsukamoto, *PNAS*, 2017, **114**, 2154-2159.

10. J. J. De Yoreo, P. U. Gilbert, N. A. Sommerdijk, R. L. Penn, S. Whitelam, D. Joester, H. Zhang, J. D. Rimer, A. Navrotsky and J. F. Banfield, *Science*, 2015, **349**.

11. Z. Sheng, H. Li, K. Du, L. Gao, J. Ju, Y. Zhang and Y. Tang, *Angew. Chem. Int. Ed.*, 2021.

12. J. Cejka, H. van Bekkum, A. Corma and F. Schueth, *Introduction to zeolite molecular sieves*, Elsevier, 2007.

13. M. E. Davis, *Ind. Eng. Chem. Res*, 1991, **30**, 1675-1683.

14. A. Chawla, R. Li, R. Jain, R. J. Clark, J. G. Sutjianto, J. C. Palmer and J. D. Rimer, *MSDE*, 2018, **3**, 159-170.

15. U. Olsbye, S. Svelle, M. Bjørgen, P. Beato, T. V. Janssens, F. Joensen, S. Bordiga and K. P. Lillerud, *Angew. Chem. Int. Ed.*, 2012, **51**, 5810-5831.

16. A. Primo and H. Garcia, *Chem. Soc. Rev.*, 2014, **43**, 7548-7561.

17. F. Su and C. Lu, *Energy Environ. Sci.*, 2012, **5**, 9021-9027.

18. S. Wang and Y. Peng, *Chem. Eng. J.*, 2010, **156**, 11-24.

19. B. M. Weckhuysen and J. Yu, *Chem. Soc. Rev.*, 2015, **44**, 7022-7024.

20. M. Dusselier and M. E. Davis, *Chem. Rev.*, 2018, **118**, 5265-5329.

21. S.-H. Lee, C.-H. Shin, D.-K. Yang, S.-D. Ahn, I.-S. Nam and S. B. Hong, *Micropor. Mesopor. Mat.*, 2004, **68**, 97-104.

22. K. Na, M. Choi and R. Ryoo, *J. Mater. Chem. A*, 2009, **19**, 6713-6719.

23. W. Park, D. Yu, K. Na, K. E. Jelfs, B. Slater, Y. Sakamoto and R. Ryoo, *Chem. Mater.*, 2011, **23**, 5131-5137.

24. S. I. Zones, K. Jayanthi, J. Pascual, D. Xie and A. Navrotsky, *Chem. Mater.*, 2021, **33**, 2126-2138.

25. R. Jain, Mallette, A.J., Rimer, J.D., *J. Am. Chem. Soc.*, 2021, **Under Revision**.

26. M. K. Choudhary, M. Kumar and J. D. Rimer, *Angew. Chem.*, 2019, **131**, 15859-15863.

27. J. D. Rimer, J. M. Fedeyko, D. G. Vlachos and R. F. Lobo, *Chem. Eur. J.*, 2006, **12**, 2926-2934.

28. J. D. Rimer, O. Trofymluk, R. F. Lobo, A. Navrotsky and D. G. Vlachos, *J. Phys. Chem. C*, 2008, **112**, 14754-14761.

29. J. D. Rimer, D. G. Vlachos and R. F. Lobo, *J. Phys. Chem. B*, 2005, **109**, 12762-12771.

30. M. Kumar, H. Luo, Y. Román-Leshkov and J. D. Rimer, *J. Am. Chem. Soc.*, 2015, **137**, 13007-13017.

31. M. K. Choudhary, R. Jain and J. D. Rimer, *PNAS*, 2020, **117**, 28632-28639.

32. A. I. Lupulescu and J. D. Rimer, *Angew. Chem.*, 2012, **124**, 3401-3405.

33. J. R. Agger, N. Pervaiz, A. K. Cheetham and M. W. Anderson, *J. Am. Chem. Soc.*, 1998, **120**, 10754-10759.

34. P. Cubillas and M.W. Anderson, *"Synthesis mechanism: Crystal growth and nucleation" in Zeolites and catalysis: synthesis, reactions and applications*, j. Cejka, A. Corma, S. Zones (Wiley-VCH, 2010), pp. 1-55.

35. M. Kumar, M. K. Choudhary and J. D. Rimer, *Nat. Commun*, 2018, **9**, 1-9.

36. K. N. Bozhilov and V. Valtchev, *Microsc. Microanal. Microstruct.*, 2019, **25**, 816-817.

37. K. N. Bozhilov, T. T. Le, Z. Qin, T. Terlier, A. Palčić, J. D. Rimer and V. Valtchev, *Sci. Adv.*, 2021, **7**, eabg0454.

38. G. Mirabello, A. Ianiro, P. H. Bomans, T. Yoda, A. Arakaki, H. Friedrich, G. de With and N. A. Sommerdijk, *Nat. Mater.*, 2020, **19**, 391-396.

39. J. D. Rimer, *Nat. Mater.*, 2020, **19**, 375-376.

40. A. Chawla, N. Linares, R. Li, J. García-Martínez and J. D. Rimer, *Chem. Mater.*, 2020, **32**, 3278-3287.

41. K. N. Olafson, R. Li, B. G. Alamani and J. D. Rimer, *Chem. Mater.*, 2016, **28**, 8453-8465.

42. M. A. Bewernitz, D. Gebauer, J. Long, H. Cölfen and L. B. Gower, *Faraday Discuss.*, 2012, **159**, 291-312.

43. L. Dai, X. Cheng and L. B. Gower, *Chem. Mater.*, 2008, **20**, 6917-6928.

44. J. Ihli, W. C. Wong, E. H. Noel, Y.-Y. Kim, A. N. Kulak, H. K. Christenson, M. J. Duer and F. C. Meldrum, *Nat. Commun*, 2014, **5**, 1-10.

45. A. S. Schenk, H. Zope, Y.-Y. Kim, A. Kros, N. A. Sommerdijk and F. C. Meldrum, *Faraday Discuss.*, 2012, **159**, 327-344.

46. P. J. Smeets, K. R. Cho, R. G. Kempen, N. A. Sommerdijk and J. J. De Yoreo, *Nat. Mater.*, 2015, **14**, 394-399.

47. L. B. Gower, *Chem. Rev.*, 2008, **108**, 4551-4627.

48. O. A. Tertuliano and J. R. Greer, *Nat. Mater.*, 2016, **15**, 1195-1202.

49. J. Ihli, Y.-W. Wang, B. Cantaert, Y.-Y. Kim, D. C. Green, P. H. Bomans, N. A. Sommerdijk and F. C. Meldrum, *Chem. Mater.*, 2015, **27**, 3999-4007.

50. M. Kumar, R. Li and J. D. Rimer, *Chem. Mater.*, 2016, **28**, 1714-1727.

51. N. Ren, B. Subotić, J. Bronić, Y. Tang, M. Dutour Sikirić, T. Mišić, V. Svetličić, S. Bosnar and T. Antonić Jelić, *Chem. Mater.*, 2012, **24**, 1726-1737.

52. R. Li, A. Chawla, N. Linares, J. G. Sutjianto, K. W. Chapman, J. G. Martínez and J. D. Rimer, *Ind. Eng. Chem. Res*, 2018, **57**, 8460-8471.

53. R. Li, N. Linares, J. G. Sutjianto, A. Chawla, J. Garcia-Martinez and J. D. Rimer, *Angew. Chem. Int. Ed.*, 2018, **57**, 11283-11288.

54. D. L. Bish and D. W. Ming, *Natural zeolites: occurrence, properties, applications*, Walter de Gruyter GmbH & Co KG, 2018.

55. G. Gottardi and E. Galli, *Natural zeolites*, Springer Science & Business Media, 2012.

56. B. G. Alamani, J. D. Gale and J. D. Rimer, *Cryst. Growth Des.*, 2021.

57. S. Farmanesh, B. G. Alamani and J. D. Rimer, *ChemComm*, 2015, **51**, 13964-13967.

58. W.-C. Huang, L.-M. Lyu, Y.-C. Yang and M. H. Huang, *J. Am. Chem. Soc.*, 2012, **134**, 1261-1267.

59. D. Wang, A. F. Wallace, J. J. De Yoreo and P. M. Dove, *PNAS*, 2009, **106**, 21511-21516.

60. Heng Dai, Jakob Claret, Eduard L Kunkes, Vivek Vattipalli, Noemi Linares, Javier García-Martinez, Ahmad Moini and J. D. Rimer, *Angew. Chem. Int. Ed. (under Revision)*.

61. D. W. Fickel, E. D'Addio, J. A. Lauterbach and R. F. Lobo, *Appl. Catal. B: Environmental*, 2011, **102**, 441-448.

62. C. Paolucci, I. Khurana, A. A. Parekh, S. Li, A. J. Shih, H. Li, J. R. Di Iorio, J. D. Albarracin-Caballero, A. Yezerets and J. T. Miller, *Science*, 2017, **357**, 898-903.

63. F. J. Machado, C. M. López, M. a. A. Centeno and C. Urbina, *Appl. Catal. A-Gen*, 1999, **181**, 29-38.

64. Y. Shen, T. T. Le, D. Fu, J. E. Schmidt, M. Filez, B. M. Weckhuysen and J. D. Rimer, *ACS Catal.*, 2018, **8**, 11042-11053.

65. A. I. Lupulescu, W. Qin and J. D. Rimer, *Langmuir*, 2016, **32**, 11888-11898.

66. H. Dai, Y. Shen, T. Yang, C. Lee, D. Fu, A. Agarwal, T. T. Le, M. Tsapatsis, J. C. Palmer and B. M. Weckhuysen, *Nat. Mater.*, 2020, **19**, 1074-1080.

67. Y. Liang, A. J. Jacobson and J. D. Rimer, *ACS Mater. Lett.*, 2020, **3**, 187-192.

68. S. D. Kim, S. H. Noh, K. H. Seong and W. J. Kim, *Micropor. Mesopor. Mat.*, 2004, **72**, 185-192.

69. S. Goel, Z. Wu, S. I. Zones and E. Iglesia, *J. Am. Chem. Soc.*, 2012, **134**, 17688-17695.

70. S. Goel, S. I. Zones and E. Iglesia, *J. Am. Chem. Soc.*, 2014, **136**, 15280-15290.

Table of Content (TOC) Graphic